Petroleum Science 20 (2023) 249–260

Contents lists available at ScienceDirect

Petroleum Science

journal homepage: www.keaipublishing.com/en/journals/petroleum-science

Original Paper

2.5-Dimensional modeling of EM logging-while-drilling tool in anisotropic medium on a Lebedev grid

Zhen-Guan Wu [a], Hu Li [b,*], Xi-Zhou Yue [c]

[a] *School of Geoscience and Technology, Southwest Petroleum University, Chengdu, Sichuan, 610500, China*
[b] *Maxwell Dynamics Inc., Houston, TX, 77074, USA*
[c] *Well-tech R & D Institute, China Oilfield Services Limited, Beijing, 101149, China*

ARTICLE INFO

Article history:
Received 12 January 2022
Received in revised form
23 June 2022
Accepted 15 September 2022
Available online 28 September 2022

Edited by Jie Hao

Keywords:
2.5D modeling
Electromagnetic logging-while-drilling
Anisotropic medium
Lebedev grid

ABSTRACT

A 2.5D finite-difference (FD) algorithm for the modeling of the electromagnetic (EM) logging-while-drilling (LWD) tool in anisotropic media is presented. The FD algorithm is based on the Lebedev grid, which allows for the discretization of the frequency-domain Maxwell's equations in the anisotropic media in 2.5D scenarios without interpolation. This leads to a system of linear equations that is solved using the multifrontal direct solver which enables the simulation of multi-sources at nearly the cost of simulating a single source for each frequency. In addition, near-optimal quadrature derived from an optimized integration path in the complex plane is employed to implement the fast inverse Fourier Transform (IFT). The algorithm is then validated by both analytic and 3D solutions. Numerical results show that two Lebedev subgrid sets are sufficient for TI medium, which is common in geosteering environments. The number of quadrature points is greatly reduced by using the near-optimal quadrature method.

© 2023 The Authors. Publishing services by Elsevier B.V. on behalf of KeAi Communications Co. Ltd. This is an open access article under the CC BY-NC-ND license (http://creativecommons.org/licenses/by-nc-nd/4.0/).

1. Introduction

Electromagnetic (EM) methods have been widely used in the field of exploration geophysics, such as controlled source electromagnetic survey (CSEM), crosswell EM method, and borehole EM logging. One of the widely-used borehole EM techniques is the directional logging-while-drilling (LWD) resistivity measurement (DRM), which provides both resistivity and boundary information for accurate geosteering (Li et al., 2005, Bell et al., 2006; Bittar et al., 2009; Hawkins et al., 2015; Omeragic et al., 2006). In recent years, the more powerful ultra-deep directional resistivity measurement has also been introduced to the industry (Seydoux et al., 2014; Hartmann et al., 2014; Wu et al., 2018; Wang et al., 2022). The new tool, which can detect 30 m or more around the borehole, enables engineers to map reservoirs for better geosteering (Antonsen et al., 2014; Thiel and Omeragic, 2017).

In geosteering, modeling and inversion are performed to help field engineers to understand the EM tools' responses and to obtain the formation resistivity profile (Pardo and Torres-Verdín, 2015; Zhou et al., 2016; Yan et al., 2020). Analytic solutions, which assume the formation model to be planarly layered with anisotropic resistivities (Hu et al., 2018; Hong et al., 2021), have been very helpful in this process. However, the DRM shows that unconformities, pinch-outs, faults, and other lateral changes appear frequently. Thus, analytic solutions are not sufficient for real-time applications. As a result, 2.5D modeling, which assumes the formation properties are arbitrarily distributed in the defined *xz*-plane but invariant along the *y*-axis, is employed in the complex scenarios (Chen et al., 2011; Dupuis et al., 2014; Zeng et al., 2018; Chaumont-Frelet et al., 2018, Wu et al., 2020).

The finite difference (FD) method is commonly used to implement the 2.5D or 3D modeling of EM responses (Abubakar et al., 2008; Lee and Teixeira, 2007, Sun and Hu, 2021). Typically, the FD scheme is cast on a staggered (Yee) grid (Yee, 1966). The advantage of the Yee grid is that in isotropic media, all the filed components are placed such that the required spatial derivatives can be calculated using second-order central differences. To extend the FD scheme based on the Yee grid to handle anisotropic media, one must interpolate the electric field components at an electric field node from the values of neighboring nodes. However, there are some disadvantages to using such an interpolation strategy

* Corresponding author.
E-mail address: lh19870205@gmail.com (H. Li).

https://doi.org/10.1016/j.petsci.2022.09.010
1995-8226/© 2023 The Authors. Publishing services by Elsevier B.V. on behalf of KeAi Communications Co. Ltd. This is an open access article under the CC BY-NC-ND license (http://creativecommons.org/licenses/by-nc-nd/4.0/).

(Davydycheva et al., 2003), such as 1) the interpolation strategy reduces the accuracy of the FD scheme; and 2) the interpolation strategy destroys the duality between the electric and magnetic fields.

The Lebedev grid is an alternative to the Yee grid (Lebedev, 1964). No interpolations are needed when using this grid, since all the electric-field components are collocated. Furthermore, the Lebedev grid can better represent materials with planar discontinuities. The 3D modeling of an EM logging tool using the Lebedev grid has been implemented by Davydycheva et al. (2003) in Cartesian coordinates. The number of unknowns is four times of those of standard Yee grids, since the Lebedev grids can be decomposed into four shifted Yee grids. However, Davydycheva et al. (2003) has shown that due to the property of error cancellation, the cell sizes can be much coarser than those using standard Yee grids. Therefore, compared to the traditional staggered grid, the Lebedev grid shows two advantages: (1) it requires no interpolation to calculate the magnetic fields (electric fields) from electric fields (magnetic fields); (2) it can be more efficient by taking the advantage of error cancelation.

In this paper, we present a 2.5D FD algorithm based on the Lebedev grid to model the responses of the DRM. We will focus on the transverse isotropic (TI) medium, which is the most common case in geosteering. A well may penetrate the formation with an arbitrary dip angle. It is shown that instead of using four Lebedev subgrids, only two subgrids are needed in TI medium. We also show that using the standard Lebedev grid, this method can be extended to full anisotropic medium readily. The remainder of this paper is organized as follows. Section II presents the theory, the Lebedev grid, and the considerations in numerical implementation. Section III will focus on the near-optimal quadrature method. Section IV provides experimental results to validate the proposed algorithm and to showcase its performance. Section V is dedicated to the conclusions.

2. Theory

2.1. Maxwell's equations in anisotropic medium

We formulate the problem in the frequency domain with the time convention $e^{-i\omega t}$. The Maxwell's equations with electric and magnetic current sources in anisotropic media can be expressed as

$$\nabla\times\boldsymbol{E} = i\omega\boldsymbol{\mu}\boldsymbol{H} - \boldsymbol{M} \tag{1a}$$

$$\nabla\times\boldsymbol{H} = -i\omega\boldsymbol{\varepsilon}^{*}\boldsymbol{E} + \boldsymbol{\sigma}\boldsymbol{E} + \boldsymbol{J}_s = -i\omega\boldsymbol{\varepsilon}\boldsymbol{E} + \boldsymbol{J}_s \tag{1b}$$

Here, $\boldsymbol{E}$ and $\boldsymbol{H}$ are the electric and magnetic fields, respectively, and $\boldsymbol{J_s}$ and $\boldsymbol{M}$ are the electric and magnetic current sources, respectively. $\boldsymbol{\mu}$ is the permeability, which is commonly assumed to be a scalar in borehole geophysics. ω is the angular frequency. $\varepsilon = \varepsilon^{*} + i\sigma/\omega$, ε^{*} and σ are the dielectric constant and conductivity tensors in ($x'y'z'$) coordinate (as shown in Fig. 1). The formation is defined in the primed coordinates ($x'y'z'$), which has a relative dip angle α with respect to the unprimed coordinates (xyz) (see Fig. 1).

$$\boldsymbol{\varepsilon} = \begin{bmatrix} \boldsymbol{\varepsilon}_{xx} & 0 & \boldsymbol{\varepsilon}_{xz} \\ 0 & \boldsymbol{\varepsilon}_{yy} & 0 \\ \boldsymbol{\varepsilon}_{zx} & 0 & \boldsymbol{\varepsilon}_{zz} \end{bmatrix} = \begin{bmatrix} \boldsymbol{\varepsilon}^{*}_{xx} + i\sigma_{xx}/\omega & 0 & \boldsymbol{\varepsilon}^{*}_{xz} + i\sigma_{xz}/\omega \\ 0 & \boldsymbol{\varepsilon}^{*}_{yy} + i\sigma_{yy}\big/\omega & 0 \\ \boldsymbol{\varepsilon}^{*}_{zx} + i\sigma_{zx}/\omega & 0 & \boldsymbol{\varepsilon}^{*}_{zz} + i\sigma_{zz}/\omega \end{bmatrix} \tag{2}$$

The TI medium is taken here as an example. The formation coordinates are denoted as ($x'y'z'$). We cast the FD scheme on a Cartesian coordinate (Fig. 1), denoted as (xyz), which is obtained by rotating the $x'y'z'$ coordinates with a dip angle α along with the y-axis. The x-axis is coincident with the projection of well trajectory in the $x'z'$ plane. A relative angle β may exist between the well trajectory and the x-axis, which indicates the y coordinates of the transmitter and receiver antennas may not be zero. The complex dielectric constant tensor in the formation coordinates (($x'y'z'$) coordinate) is given by:

$$\bar{\boldsymbol{\varepsilon}} = \begin{bmatrix} \boldsymbol{\varepsilon}_h & 0 & 0 \\ 0 & \boldsymbol{\varepsilon}_h & 0 \\ 0 & 0 & \boldsymbol{\varepsilon}_v \end{bmatrix} = \begin{bmatrix} \boldsymbol{\varepsilon}^{*}_h + i\sigma_h/\omega & 0 & 0 \\ 0 & \boldsymbol{\varepsilon}^{*}_h + i\sigma_h/\omega & 0 \\ 0 & 0 & \boldsymbol{\varepsilon}^{*}_v + i\sigma_v/\omega \end{bmatrix} \tag{3}$$

In the unprimed coordinates, the complex dielectric constant tensor can be expressed as:

$$\boldsymbol{\varepsilon} = \boldsymbol{R}^{-1}\bar{\boldsymbol{\varepsilon}}\boldsymbol{R} \tag{4}$$

Here, $\boldsymbol{R}$ is the rotation matrix relative to the dip angle α. $\boldsymbol{R}$ is given by:

$$\boldsymbol{R}(\alpha) = \begin{bmatrix} \cos\alpha & 0 & -\sin\alpha \\ 0 & 1 & 0 \\ \sin\alpha & 0 & \cos\alpha \end{bmatrix} \tag{5}$$

Thus, the complex dielectric constant tensor provided in Eq. (2) would be sufficient to describe most scenarios in borehole geophysics, such as TI medium and biaxial anisotropic medium, especially in 2.5D cases.

Eliminating $\boldsymbol{H}$ from Eq. (1), we obtain:

$$\nabla\times\nabla\times\boldsymbol{E} - \boldsymbol{k}^2\boldsymbol{E} = i\omega\mu\boldsymbol{J}_s - \nabla\times\boldsymbol{M} \tag{6}$$

Here, $\boldsymbol{k^2} = \omega^2\varepsilon\mu$. Eq. (6) can be discretized according to the finite-difference approach. To take advantage of the 2D structure of the configuration (invariant along the y-axis), we introduce the 1D spatial Fourier Transform and its inverse with respect to the y-coordinate axis:

$$\tilde{u}(x,k_y,z) = F\{u\} = \int_{y=-\infty}^{\infty} \mathrm{d}y e^{ik_y y} u(x,y,z) \tag{7}$$

and the inverse transform:

$$u(x,y,z) = F^{-1}\{\tilde{u}\} = \frac{1}{2\pi}\int_{k_y=-\infty}^{\infty} \mathrm{d}y e^{-ik_y y}\tilde{u}(x,k_y,z) \tag{8}$$

Applying the Fourier transforms to Eq. (6), we obtain:

$$\overline{\nabla}\times\overline{\nabla}\times\overline{\boldsymbol{E}} - \boldsymbol{k}^2\overline{\boldsymbol{E}} = i\omega\mu\overline{\boldsymbol{J}_s} - \overline{\nabla}\times\overline{\boldsymbol{M}} \tag{9}$$

Here $\overline{\nabla} = \partial/\partial x\,\vec{e}_x + ik_y\vec{e}_y + \partial/\partial z\,\vec{e}_z$. $\overline{\boldsymbol{E}}$, $\overline{\boldsymbol{J}_s}$, and $\overline{\boldsymbol{M}}$ represent the electric field, current source, and magnetic source in the spectral domain, respectively.

Using the definition of the curl operator and considering that all the y-related conductivities (except $\square_{yy}$) are zero, Eq. (9) can be decomposed into three equations:

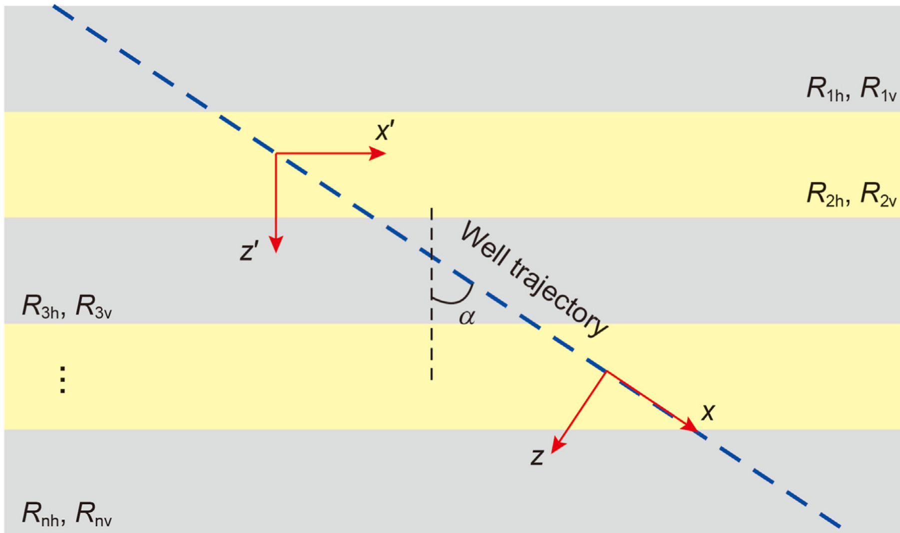

Fig. 1. Illustration of the coordinates used to describe the well trajectory and formation.

$$k_y^2\overline{E}_x - \frac{\partial^2}{\partial z^2}\overline{E}_x + ik_y\frac{\partial}{\partial x}\overline{E}_y + \frac{\partial^2}{\partial x\partial z}\overline{E}_z - \omega^2\mu[\varepsilon_{xx}\overline{E}_x + \varepsilon_{xz}\overline{E}_z] = i\omega\mu\overline{J}_x - \left[ik_y\overline{M}_z - \frac{\partial}{\partial z}\overline{M}_y\right] \tag{10a}$$

$$ik_y\frac{\partial}{\partial x}\overline{E}_x - \frac{\partial^2}{\partial x^2}\overline{E}_y - \frac{\partial^2}{\partial z^2}\overline{E}_y + ik_y\frac{\partial}{\partial z}\overline{E}_z - \omega^2\mu\boldsymbol{\varepsilon}_{yy}\overline{E}_y = i\omega\mu\overline{J}_y - \left[\frac{\partial}{\partial z}\overline{M}_x - \frac{\partial}{\partial x}\overline{M}_z\right] \tag{10b}$$

$$\frac{\partial^2}{\partial x\partial z}\overline{E}_x + ik_y\frac{\partial}{\partial z}\overline{E}_y - \frac{\partial^2}{\partial x^2}\overline{E}_z + k_y^2\overline{E}_z - \omega^2\mu[\boldsymbol{\varepsilon}_{zx}\overline{E}_x + \boldsymbol{\varepsilon}_{zz}\overline{E}_z] = i\omega\mu\overline{J}_z - \left[\frac{\partial}{\partial x}\overline{M}_y - ik_y\overline{M}_x\right] \tag{10c}$$

Upon discretization, we obtain the FD counterpart of Eq. (9), written in matrix notation as:

$$\overline{\boldsymbol{A}}\cdot\overline{\boldsymbol{x}} = \overline{\boldsymbol{b}}, \tag{11}$$

where $\overline{\boldsymbol{A}}$ is a stiffness matrix resulting from the left side of Eq. (9), $\overline{\boldsymbol{x}}$ is a vector containing the electric field at all nodes, and $\overline{\boldsymbol{b}}$ is a vector resulting from the right side of Eq. (9) at all nodes. After solving Eq. (11), the electric and the magnetic field vectors at the FD nodes can be obtained from:

$$\boldsymbol{E}(x,y,z) = \frac{1}{2\pi}\int_{k_y=-\infty}^{\infty} dk_y e^{-ik_y y}\overline{\boldsymbol{E}}(x,k_y,z) \tag{12a}$$

$$\boldsymbol{H}(x,y,z) = \frac{1}{i\omega\mu}\nabla\times\boldsymbol{E}(x,y,z) \tag{12b}$$

2.2. 2.5D Lebedev grids

We introduce the 2.5D Cartesian coordinates:

$$(x_i,\widehat{x}_i,z_k,\widehat{z}_k), i=1,\cdots M_x+1 \quad k=1,\cdots M_z+1$$
$$\text{where}\quad x_1=\widehat{x}_1 \quad z_1=\widehat{z}_1 \quad x_i<\widehat{x}_{i+1}<x_{i+1} \quad z_k<\widehat{z}_{k+1}<z_{k+1} \tag{13}$$

Here, M_x+1, and M_z+1 are the maximum node number in x, and z directions, respectively. We denote x_i and z_k to be the primary-grid nodes, and $\widehat{x}_i$ and $\widehat{z}_k$ to be the dual-grid nodes. The unknown fields of $\boldsymbol{E}$ and $\boldsymbol{H}$ are determined by the method of FDs on this 2.5D Lebedev grid. In this grid, the E_x, E_z, H_x, and H_z (Non$y$-) components are collocated, but staggered half a spatial step by the E_y and H_y components (Fig. 2). We assign all Non$y$-components to nodes denoted as (x_i,z_k) and $(\widehat{x}_i,\widehat{z}_k)$, and y-components to nodes denoted as $(x_i,\widehat{z}_k)$ and $(\widehat{x}_i,z_k)$.

We consider the standard Yee grid where the $\boldsymbol{E}$ and $\boldsymbol{H}$ components have the indices:

$$\begin{aligned}&E_x(x_i,z_k), E_y(\widehat{x}_{i+1},z_k), E_z(\widehat{x}_{i+1},\widehat{z}_{k+1})\\&H_x(\widehat{x}_{i+1},\widehat{z}_{k+1}), H_y(x_i,\widehat{z}_{k+1}), H_z(x_i,z_k)\end{aligned} \tag{14}$$

We call this Yee grid "subgrid 1", and the other grid, which is constructed from the standard Yee grid by shifting the components of $\boldsymbol{E}$ and $\boldsymbol{H}$ by $h_{xi}/2$, and $h_{zk}/2$, respectively, in the $(\pm)$ x- and $(\pm)$ z-directions, "subgrid 2". On subgrid 2, the components of $\boldsymbol{E}$ and $\boldsymbol{H}$ have the indices:

$$\begin{aligned}&E_x(\widehat{x}_{i+1},\widehat{z}_{k+1}), E_y(x_i,\widehat{z}_{k+1}), E_z(x_i,z_k)\\&H_x(x_i,z_k), H_y(\widehat{x}_{i+1},z_k), H_z(\widehat{x}_{i+1},\widehat{z}_{k+1})\end{aligned} \tag{15}$$

Superposition of these two subgrids results in the 2.5D Lebedev grid, denoted as Lebedev grid A. If the off-diagonal elements of the complex dielectric constant tensor are non-zero, these two subgrids are coupled. Otherwise, if only diagonal elements are non-zero, these two subgrids are decoupled. Furthermore, the E_y components of the two subgrids are always decoupled, since y-related conductivities (except yy component) are all zero.

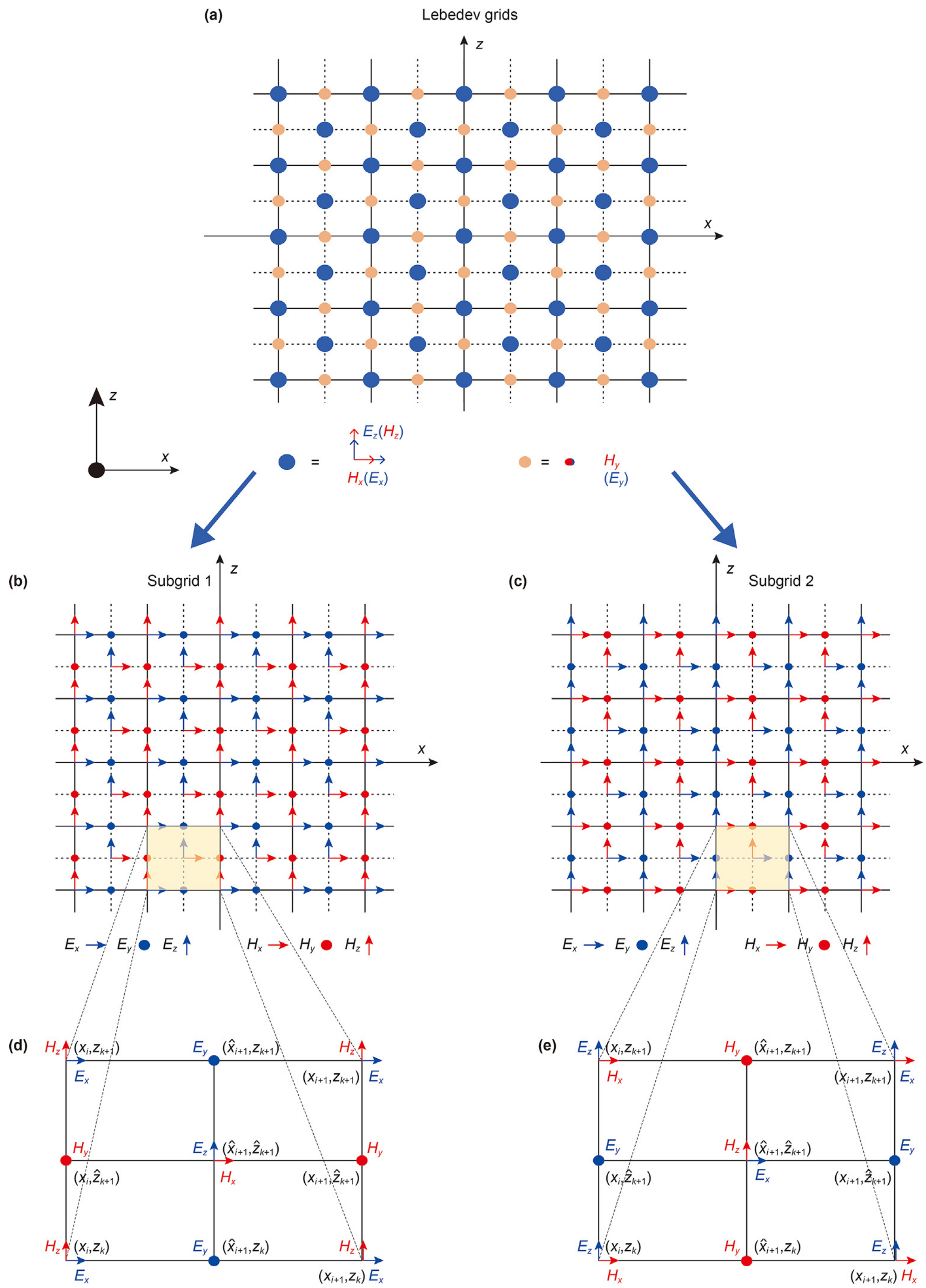

Fig. 2. Illustration of the Lebedev grid on 2.5D Cartesian coordinates. The E_x, E_z, H_x, and H_z (Nony-) components are collocated, but half a spatial step staggered by the E_y and H_y components. We assign all Nony-components to nodes denoted as (x_i, z_k) and $(\hat{x}_i, \hat{z}_k)$, and y-components to nodes denoted as $(x_i\, \hat{z}_k)$ and $(\hat{x}_i, z_k)$. (d) is the standard Yee grid, while (e) can be regarded as the standard grid shifting $h_x/2$ and $h_z/2$ in x and z directions.

2.3. Extension to arbitrary anisotropic medium

The above grids can be extended to an arbitrary anisotropic medium by introducing a shifted Lebedev grid B (as shown in Fig. 3). Lebedev grid can be regarded as shifting the grid A $h_{xi}/2$, and $h_{zk}/2$ in the ($\pm$) x- and ($\pm$) z-directions, respectively. Grids A and B comprise the complete Lebedev grid, in which all the ***E*** and ***H*** components are collocated, and thus, can handle arbitrary resistivity (conductivity) anisotropy. In the full anisotropic medium, Eq. (10) can be rewritten as:

$$\begin{aligned} &k_y^2\overline{E}_x - \frac{\partial^2}{\partial z^2}\overline{E}_x + ik_y\frac{\partial}{\partial x}\overline{E}_y + \frac{\partial^2}{\partial x \partial z}\overline{E}_z \\ &-\omega^2\mu\left[\varepsilon_{xx}\overline{E}_x + \varepsilon_{xy}\overline{E}_y + \varepsilon_{xz}\overline{E}_z\right] = i\omega\mu\overline{J}_x - \left[ik_y\overline{M}_z - \frac{\partial}{\partial z}\overline{M}_y\right] \end{aligned} \tag{16a}$$

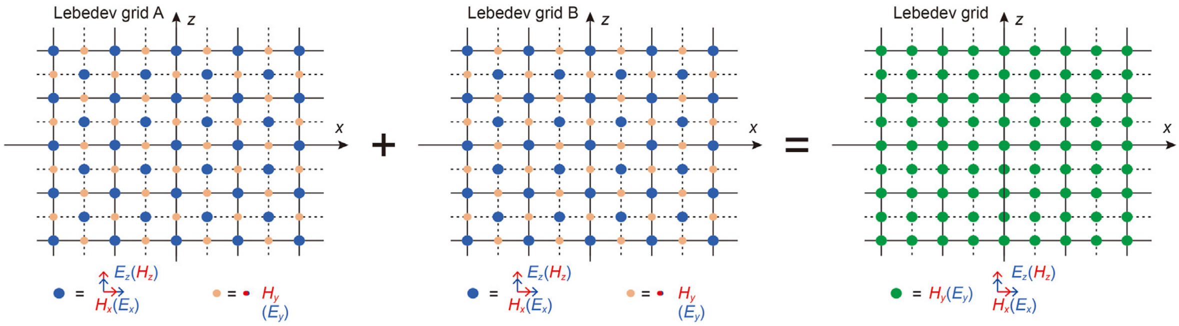

Fig. 3. Illustration of the Lebedev grid in an arbitrary anisotropic medium. left: grid A as described above; middle: grid B, which can be regarded as grid A shifts $h_{xi}/2$ and $h_{zk}/2$ in the x and z directions, respectively. Grids A and B comprise the complete Lebedev grid, which can handle arbitrary anisotropy. In the complete Lebedev grid, all the ***E*** and ***H*** components are collocated.

$$
\begin{aligned}
& ik_y\frac{\partial}{\partial x}\overline{E}_x-\frac{\partial^2}{\partial x^2}\overline{E}_y-\frac{\partial^2}{\partial z^2}\overline{E}_y+ik_y\frac{\partial}{\partial z}\overline{E}_z \\
& -\omega^2\mu\left[\boldsymbol{\varepsilon}_{yx}\overline{E}_x+\boldsymbol{\varepsilon}_{yy}\overline{E}_y+\boldsymbol{\varepsilon}_{yz}\overline{E}_z\right]=i\omega\mu\overline{J}_y-\left[\frac{\partial}{\partial z}\overline{M}_x-\frac{\partial}{\partial x}\overline{M}_z\right]
\end{aligned} \tag{16b}
$$

$$
\begin{aligned}
& \frac{\partial^2}{\partial x\partial z}\overline{E}_x+ik_y\frac{\partial}{\partial z}\overline{E}_y-\frac{\partial^2}{\partial x^2}\overline{E}_z+k_y^2\overline{E}_z \\
& -\omega^2\mu\left[\boldsymbol{\varepsilon}_{zx}\overline{E}_x+\boldsymbol{\varepsilon}_{zy}\overline{E}_z+\boldsymbol{\varepsilon}_{zz}\overline{E}_z\right]=i\omega\mu\overline{J}_z-\left[\frac{\partial}{\partial x}\overline{M}_y-ik_y\overline{M}_x\right]
\end{aligned} \tag{16c}
$$

Here, all the $\overline{E}_x$, $\overline{E}_y$, and $\overline{E}_z$ components in Eq. (16) are defined at the same location. However, one should note that, they would belong to different subgrids and Eq. (16) should be cast on all subgrids. Taking Eq. (16a) as an example, for subgrid 1 in Lebedev grid A, the left-hand side (LHS) can be expressed as:

$$
k_y^2\overline{E}_x^1-\frac{\partial^2}{\partial z^2}\overline{E}_x^1+ik_y\frac{\partial}{\partial x}\overline{E}_y^1+\frac{\partial^2}{\partial x\partial z}\overline{E}_z^1-\omega^2\mu\left[\varepsilon_{xx}\overline{E}_x^1+\varepsilon_{xy}\overline{E}_y^B+\varepsilon_{xz}\overline{E}_z^2\right] \tag{17}
$$

Here, the upper scripts of the $\overline{E}$ components are the numbers of the corresponding subgrids. Similarly, grid B can be decomposed into two subgrids. However, we will focus on Lebedev grid A (or equally grid B), in our investigation.

2.4. Numerical considerations

Geosteering in real scenarios is a full 3D problem. However, 3D forward modeling is time-consuming, and an efficient way to handle this problem is to project the 3D system into a 2D plane. The coordinates are set as illustrated in section II.A (Fig. 1). In discretization, uniform grids are used in the x and z directions within the scope of the tool (or within a depth range (a depth window) when we try to model the tool's responses inside a single segment at once) to improve the accuracy of the model. The minimum cell-sizes are 2 cm in both x and z directions. The cell sizes gradually increase to the maximum size, which is dependent on the skin depth outside of the depth window. Both the width and the height of the window are set to 1.5 times the tool length, and that is around 3.5 m for the DRM in our cases. Eq. (9) or Eq. (16) is then discretized on the proposed 2.5D Lebedev grid. This leads to a system of linear equations that can be solved using the multifrontal direct solver. The direct solver enables the simulation of multi-sources at nearly the cost of simulating a single source for each frequency. The IFT is evaluated using the near-optimal quadrature, which decays fast, to obtain the ***E*** and ***H*** components at all the nodes. The responses of DRM can then be obtained. The near-optimal quadrature method can be found in Ingerman et al. (2000) and Li et al. (2016), the details are also given in the Appendix.

3. Numerical experiments

There are generally two kinds of measurements delivered by the DRM: apparent resistivity and geosignal logs (Wang et al., 2019; Li et al., 2020). Typically, in LWD applications, a basic configuration, which comprises one coil transmitter and two coil receivers, is employed to measure the apparent resistivity logs (Fig. 4a). The phase-shift (PS) and attenuation (Att) are defined as:

$$
\mathrm{PS}=\tan^{-1}\frac{\mathrm{Im}(V_{R1})}{\mathrm{Re}(V_{R1})}-\tan^{-1}\frac{\mathrm{Im}(V_{R2})}{\mathrm{Re}(V_{R2})} \tag{18a}
$$

$$
\mathrm{Att}=-20\log_{10}\left[\frac{\mathrm{abs}(V_{R2})}{\mathrm{abs}(V_{R1})}\right] \tag{18b}
$$

where V_{R1} and V_{R2} are the voltages induced in the first and second coil receivers, respectively. The PS and Att signals are calibrated to phase-shift resistivity (RA) and attenuation resistivity (RP) logs, respectively, using a relationship established in the homogeneous medium (as shown in Fig. 5). Fig. 5 also validates the results of the 2.5D algorithm with the analytic solutions in the isotropic medium.

Commonly, a basic coaxial-transmitter, tilted-receiver configuration is employed to measure the geosignal (Fig. 4b). The phase-shift (GP) and amplitude-attenuation (GA) geosignals are calculated from the phase-shift and amplitude-ratio of two measurements with tool azimuth differing by 180° [1]. For example, we use $\beta_1=0^\circ$, $\beta_2=180^\circ$ to denote the up (x) and down (-x) directions the receiver is pointing to during rotation. The GP and GA geosignal are then defined as:

$$
\mathrm{GP}=\tan^{-1}\frac{\mathrm{Im}(V_{\beta_1})}{\mathrm{Re}(V_{\beta_1})}-\tan^{-1}\frac{\mathrm{Im}(V_{\beta_2})}{\mathrm{Re}(V_{\beta_2})} \tag{19a}
$$

$$
\mathrm{GA}=-20\log_{10}\frac{\mathrm{abs}(V_{\beta_1})}{\mathrm{abs}(V_{\beta_2})} \tag{19b}
$$

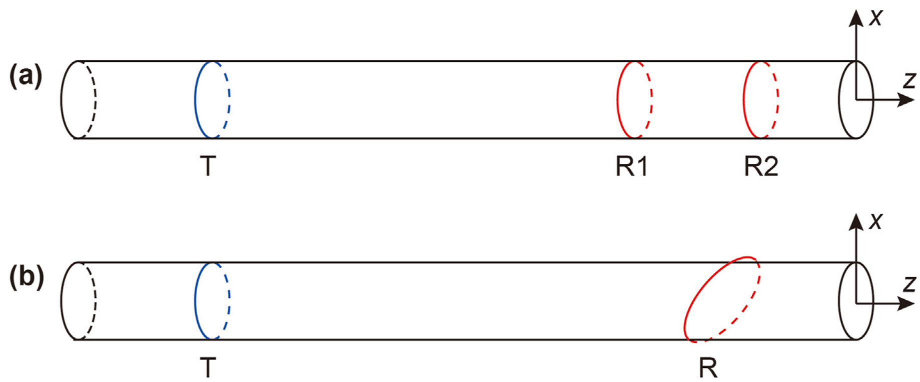

Fig. 4. Basic configurations, which can provide resistivity (above) or geosignal (below). (a) One transmitter (T) – two receivers (R) structure; (b) Axial transmitter (T) – tilted receiver (R) structure, which can deliver geosignal.

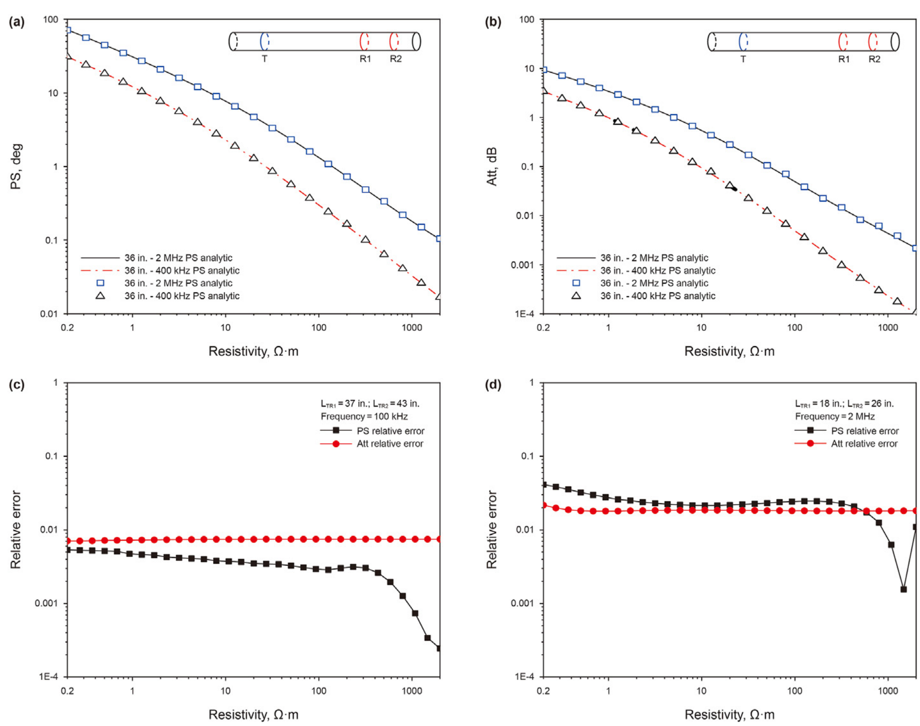

Fig. 5. Validation of the 2.5D algorithm in isotropic homogeneous medium. (a) Conversion chart for 36 in spacing, 2 MHz, and 400 kHz PS measurements; (b) Conversion chart for 36 in, 2 MHz and 400 kHz Att measurements; Relative errors between the 2.5D algorithm results and the analytical solutions (c) for 100 kHz – 40 in. configuration; (d) for 2 MHz – 22 in. configuration.

In the following of this section, we will validate the proposed 2.5D method in the TI medium, the full anisotropic medium, and layered anisotropic medium. Then, the responses of DRM in a complex fault structure are simulated.

In the following of this section, we will validate the proposed 2.5D method in the TI medium, the full anisotropic medium, and layered anisotropic medium. Then, the responses of DRM in a complex fault structure are simulated.

3.1. Validation in the transverse isotropic (TI) medium

The ***H*** components are modeled using the 2.5D algorithm in the TI medium and validated against the analytic solutions (Løseth and Ursin, 2007; Hong et al., 2013). A single transmitter-receiver pair, with a spacing of 2 m, is in a homogeneous TI medium. The transmitter and receiver are assumed to be magnetic dipoles. Fig. 6 presents all the ***H*** components induced in the receiver dipole when the transmitter is radiating a 100 kHz time harmonic signal. In this case, the horizontal and vertical resistivities are 1.0 Ω m and 10.0 Ω m respectively. The transmitter and receiver are both set to be magnetic dipoles, and the positions are −1.0 m and 1.0 m, respectively. The tool operation frequency is 100 kHz. The *x*-axis is the relative dip angle between the tool and the horizontal resistivity direction. The good agreement between the 2.5D results and analytic solutions indicates the effectiveness of the proposed method in the TI medium.

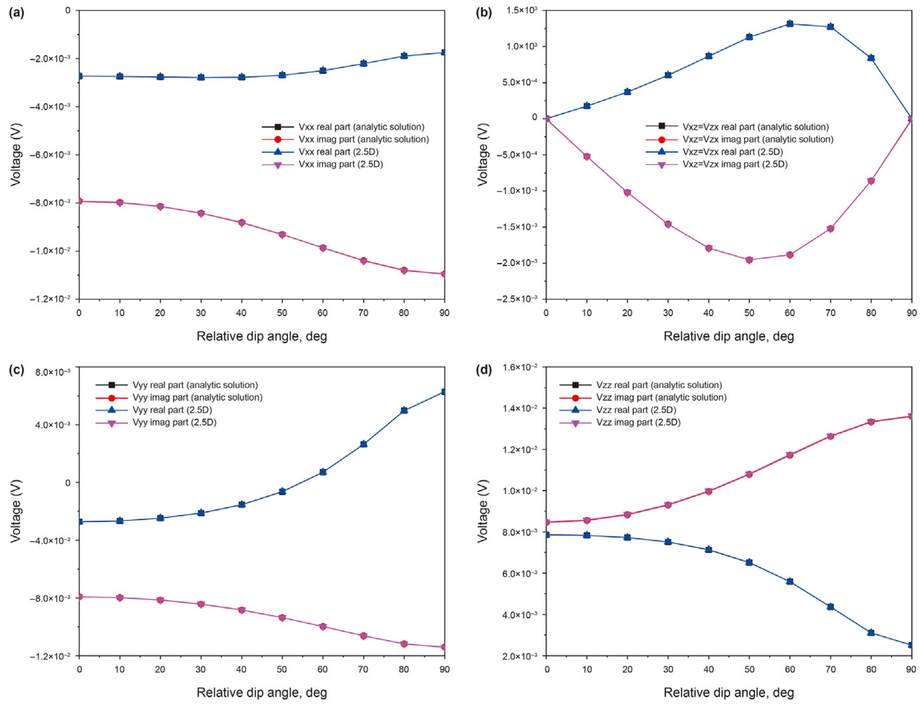

Fig. 6. The ***H*** components responses vs. dip angle in TI medium. (a) V_{xx} component; (b) V_{xz} and V_{zx} components; (c) V_{yy} components; (d) V_{zz} components. The first and second subscripts are the directions of the transmitter and receiver, respectively.

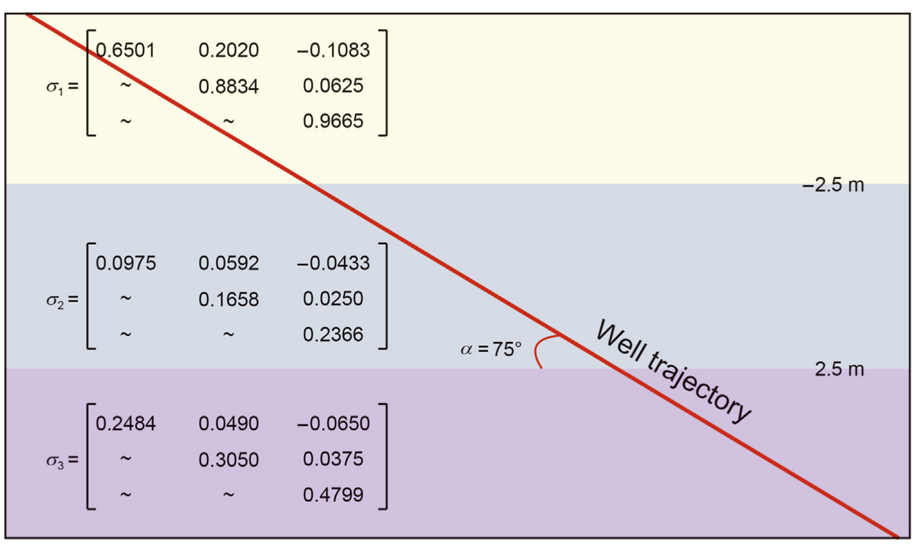

Fig. 7. A three-layer full anisotropic model.

3.2. Validation in the full anisotropic medium

As illustrated in subsection II.C, the proposed method can be easily extended to the full anisotropic medium. We established a three-layer model whose conductivity tensors are full anisotropic, meaning all the elements are non-zero. The upper and lower layers are semi-infinite and the middle layer is 5 m thick. A well penetrates the model with a 75° relative dip angle (Fig. 7). All the three layers are full anisotropic. Note that though some elements in the conductivity tensor are negative, they remain positive-defined matrices. The transmitter and receiver are assumed to be magnetic dipoles, with a spacing of 2 m. The tool operation frequency is 100 kHz. The simulated results are shown in Fig. 8, validated with the results computed using a commercial software with a 3D model. Note that the first and second subscripts of the components are the directions of the transmitter and receiver dipoles, respectively.

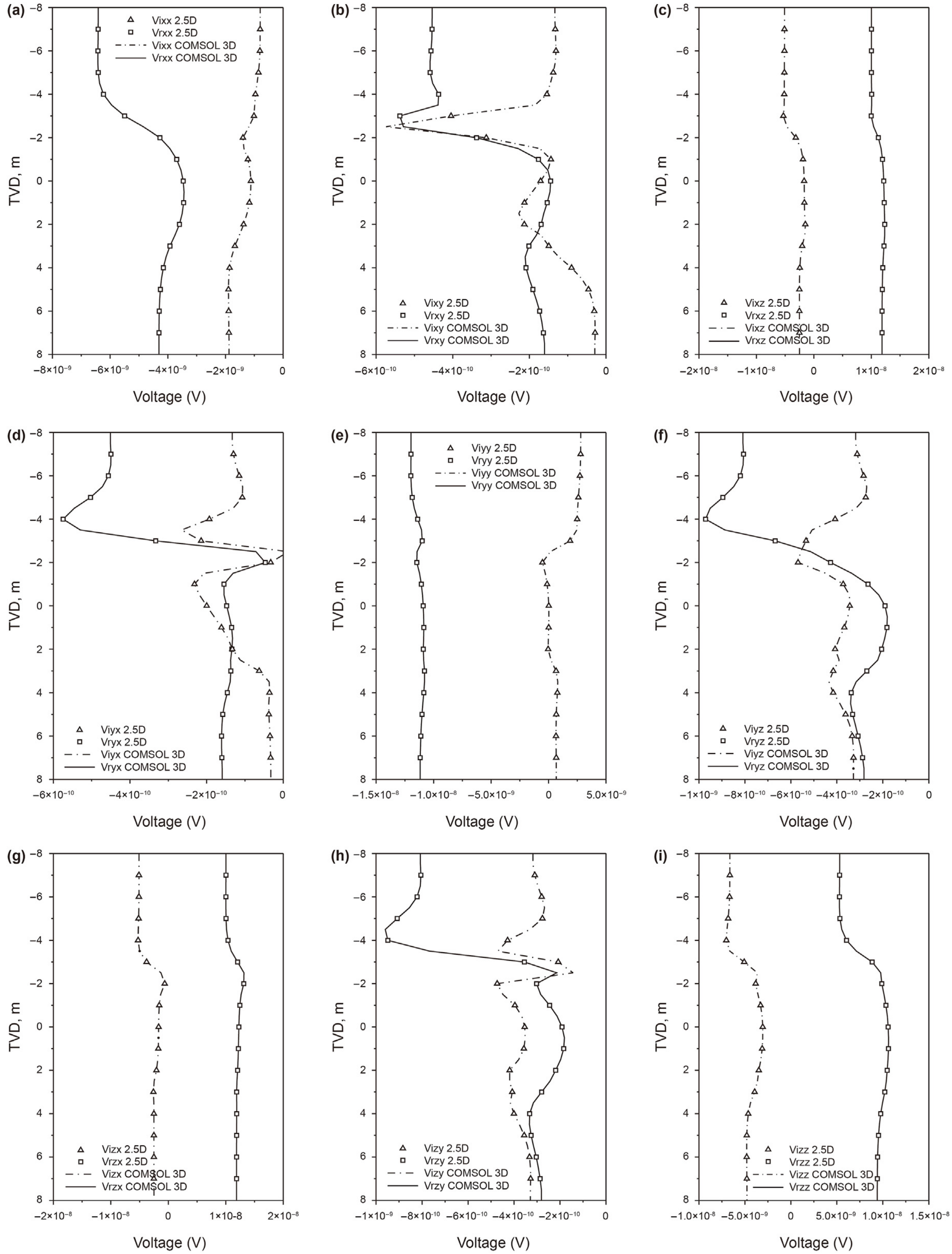

Fig. 8. Validation of 2.5D FD code in full anisotropic medium.

Table 1
Parameters of Oklahoma formation model used in Fig. 9. NL represents the number of layer, H is the thickness of the layer and R_h (R_v) is the horizontal (vertical) resistivity of the layer.

NL	H, m	R_h, Ω·m	R_v, Ω·m	NL	H, m	R_h, Ω·m	R_v, Ω·m	NL	H, m	R_h, Ω·m	R_v, Ω·m
1	3.716	1	1	10	1.524	120	300	19	1.524	7.5	30
2	5.486	10	30	11	2.134	4	20	20	1.229	0.9	0.9
3	2.438	0.4	2	12	5.486	150	500	21	1.219	2	10
4	1.219	3	10	13	2.438	40	40	22	1.219	10	30
5	0.914	0.9	5	14	2.134	1.5	1.5	23	0.914	1.8	5
6	2.134	20	50	15	2.743	100	300	24	0.610	20	100
7	1.219	0.7	3	16	1.524	18	18	25	0.610	7.5	7.5
8	1.829	100	200	17	1.219	100	200	26	0.610	15	80
9	0.914	6.5	20	18	0.914	1.5	5	27	2.088	0.7	0.7

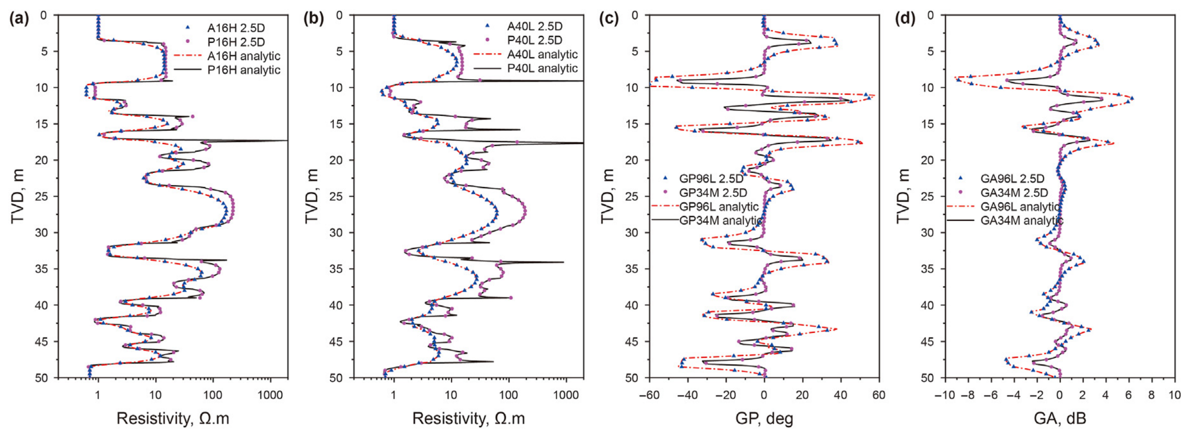

Fig. 9. The responses of DRM in Oklahoma (OK) model. (a) 16 in – 2 MHz PS and Att resistivities; (b) 40 in – 400 kHz PS and Att resistivities; (c) 34 in – 400 kHz and 96 in – 100 kHz GP signal; (d) 34 in – 400 kHz and 96 in – 100 kHz GA signal. The parameters of the formation are listed in Table 1. H, L, and M represent the high frequency, low frequency, and medium frequency, respectively.

3.3. DRM's responses in a planarly layered model

In this subsection, we simulate the responses of a typical DRM tool, which can provide multiple resistivity and geosignal logs, using the proposed method in a more realistic “Oklahoma” (OK) formation model. The OK model consists of a set of alternating conductive and resistive layers (27 in total) with thicknesses (D) ranging from 0.6 m to 5.5 m (as shown in Table 1). Resistivity varies from 0.4 Ω m to 500 Ω m. The upper and lower layers are assumed to be semi-infinite. The relative dip angle between the well and the formation is 75°. We employed a 3.5 m length depth window, which enables us to model multiple measure points at the same time (four points if the spacing is set to 0.2 m in true-vertical-depth (TVD)). The computational domain is a 5δ × 5δ rectangle (δ represents the skindepth), it is composed of two parts: the depth window and the remaining domain outside the window. Within the window, uniform grids are used, while outside the window, non-uniform meshes are adopted. The tool has three operation frequencies: 2 MHz, 400 kHz, and 100 kHz. The direct solver enables the simulation of each frequency in a depth window, which includes a total of nearly 100 transmitter-receiver pairs, in 20 s on an i7-6600U processor. Validation by analytic solutions shows that the proposed method can handle high-contrast conductivity profile as well as thick layers (see Fig. 9).

3.4. Fault model

To further showcase the performance of the proposed method, we simulate the responses of DRM in a fault-structure model (Fig. 10a). A similar model is used by Chaumont-Frelet et al. (2018). The model contains a 5 m thick layer that is partially saturated with oil (above) and water (below). The layer has a 6° dip angle (θ_1) with respect to the x'-direction. The model features two geophysical faults, which have a relative angle $\theta_2 = 40°$ with respect to the z'-direction, which are separated by 20 m. The oil and water-bearing layers and both the upper and lower shoulders are anisotropic. The resistivities are shown in Fig. 10a. A synthetic well drills into the reservoir, tracks the oil-bearing layer, and penetrates both faults. The inclination of the well trajectory ranges from 55° to 120°. The resistivities and geosignals are presented in Fig.10b to d. It shows that the proposed method can accommodate complex geologic structures as well as complex geometric relationships between the formation and the well trajectory.

4. Conclusion

In this paper, we presented a 2.5D Finite-Difference (FD) algorithm based on the Lebedev grid to model the responses of directional logging-while-drilling (LWD) resistivity measurement

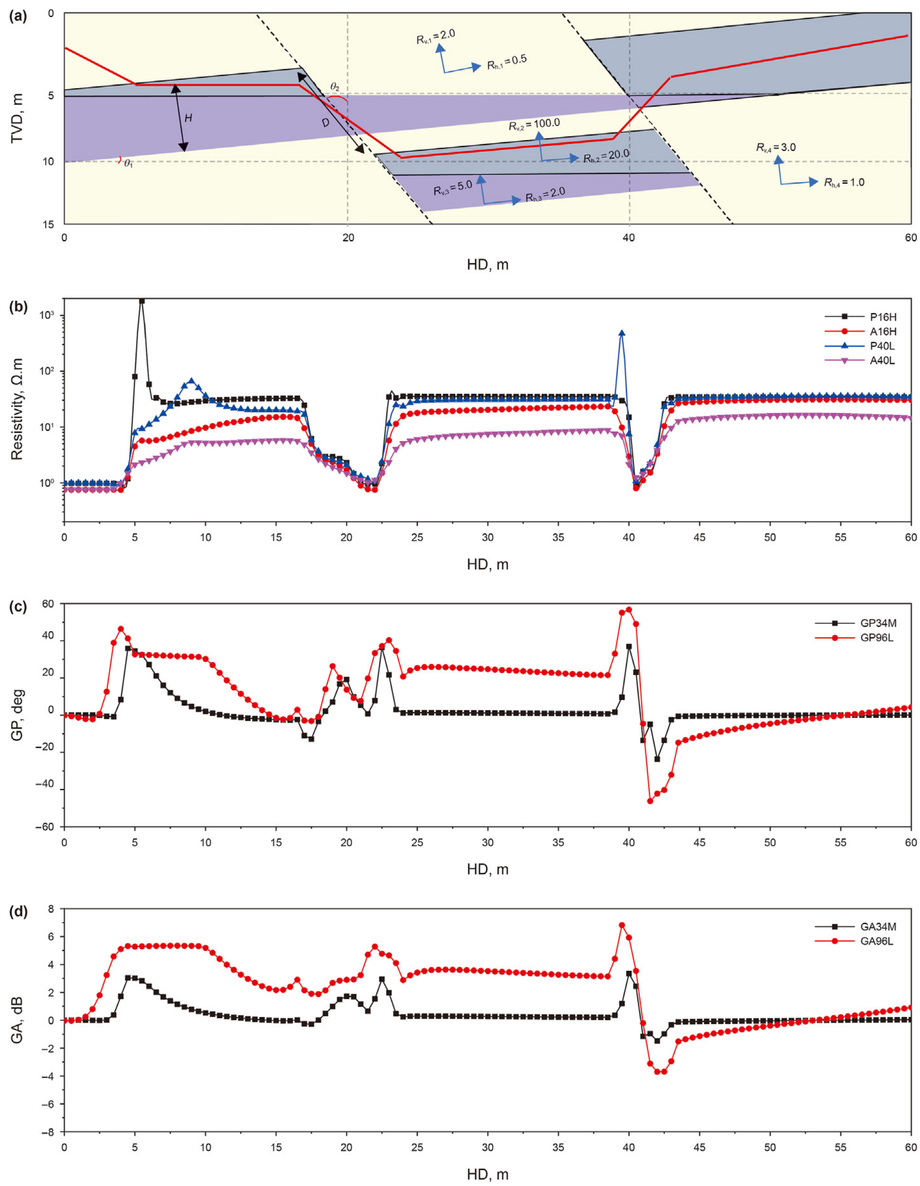

Fig. 10. The fault model and corresponding DRM responses. (a) the fault formation and well trajectory; (b) the 16 in – 2 MHz PS and Att resistivities and 40 in – 400 kHz PS and Att resistivities; (c) 34 in – 400 kHz and 96 in – 100 kHz GP signal; (d) 34 in – 400 kHz and 96 in – 100 kHz GA signal.

(DRM). We have shown that in borehole electromagnetic (EM) applications, two subgrids are sufficient for 2.5D anisotropic scenarios. Furthermore, the method can be easily extended to the full anisotropic media. The near-optimal quadrature method is used to achieve the fast inversion Fourier Transform. Numerical examples show that the 2.5D FD algorithm based on Lebedev is accurate for DRM modeling. By using the depth window strategy, the efficiency improves significantly since the simulation of multi-sources at nearly the cost of simulating a single source for each frequency. We have to emphasize that the 2.5D Lebedev grid is a considerable approach for EM modeling even though it may lead to more unknowns than the traditional Yee grid.

Acknowledgements

This work was sponsored by CNPC Innovation Found (2021DQ02-0401-0401), China Postdoctoral Science Foundation (No. 2022MD713806) and National Key R&D Program of China (2019YFA0708301).

APPENDIX

Near-optimal Quadrature for fast IFT.

In this appendix, we derive the near-optimal quadrature method needed to convert the spectral domain field to the spatial domain.

Eq. (6) in full anisotropic medium can be expressed as

$$\nabla \times \nabla \times \boldsymbol{E} - \omega^2 \varepsilon \mu \boldsymbol{E} = i\omega\mu \boldsymbol{J}_s - \nabla \times \boldsymbol{M}, \tag{A-1}$$

In Cartesian coordinates, Eq. (A-1) can be expressed as

$$\frac{\partial^2}{\partial y^2}\boldsymbol{E}(x,y,z) = \boldsymbol{T}\cdot\boldsymbol{E}(x,y,z) - \boldsymbol{F}(x,y,z), \tag{A-2}$$

Here, $\boldsymbol{F} = i\omega\mu \boldsymbol{J}_s - \nabla \times \boldsymbol{M}$,

$$\boldsymbol{T} = \begin{bmatrix} -\frac{\partial^2}{\partial z^2} & \frac{\partial^2}{\partial x \partial y} & \frac{\partial^2}{\partial x \partial z} \\ \frac{\partial^2}{\partial x \partial y} & -\frac{\partial^2}{\partial x^2} + \frac{\partial^2}{\partial x^2} - \frac{\partial^2}{\partial z^2} & \frac{\partial^2}{\partial y \partial z} \\ \frac{\partial^2}{\partial x \partial z} & \frac{\partial^2}{\partial y \partial z} & \frac{\partial^2}{\partial x^2} \end{bmatrix} - \omega^2 \mu \begin{bmatrix} \varepsilon_{xx} & \varepsilon_{xy} & \varepsilon_{xz} \\ \varepsilon_{yx} & \varepsilon_{yy} & \varepsilon_{yz} \\ \varepsilon_{zx} & \varepsilon_{zy} & \varepsilon_{zz} \end{bmatrix}, \tag{A-3}$$

By applying the Fourier transform, Eq. (A-2) becomes:

$$-k_y^2 \overline{\boldsymbol{E}}(x,k_y,z) = \overline{\boldsymbol{T}}(k_y)\cdot\overline{\boldsymbol{E}}(x,k_y,z) - \overline{\boldsymbol{F}}(x,k_y,z), \tag{A-4}$$

where $\overline{\boldsymbol{T}}(k_y)$,$\overline{\boldsymbol{F}}(x,k_y,z)$ are the Fourier transforms of $\boldsymbol{T}$, and $\boldsymbol{F}$. By substituting Eq. (12a) to Eq.(A-4), we have:

$$\boldsymbol{E}(x,0,z) = \frac{1}{4\pi i}\int_{-\infty}^{\infty} \mathrm{d}s \frac{1}{\sqrt{s}}\left[s\boldsymbol{I} - \overline{\boldsymbol{T}}(i\sqrt{s})\right]^{-1}\overline{\boldsymbol{F}}(x, i\sqrt{s}, z), \tag{A-5}$$

where $\sqrt{s} = -ik_y$. Using rational function (Ingerman et al., 2000; Li et al., 2016); i.e.

$$\frac{1}{\sqrt{s}} = \sum_{n=1}^{N}\frac{w_n}{s - s_n}, \tag{A-6}$$

where s_n and w_n represent the sampling points and the weight, respectively. Substituting Eq. (A-6) into Eq. (A-5) and applying the residue theorem, we have:

$$\begin{aligned}\boldsymbol{E}(x,0,z) &= \frac{1}{4\pi i}\sum_{n=1}^{N} w_n \overline{\boldsymbol{E}}(x, i\sqrt{s_n}, z) \\ &= \sum_{n=1}^{N} w_n\left[s_n\boldsymbol{I} - \overline{\boldsymbol{T}}(i\sqrt{s_n})\right]^{-1}\overline{\boldsymbol{F}}(x, i\sqrt{s_n}, z),\end{aligned} \tag{A-7}$$

here $\overline{\boldsymbol{E}}(x, i\sqrt{s_n}, z)$ represents the solutions of the 2D problem in Fourier Domain. In this paper, we use the two-interval strategy and the Pade approximation to approximate the square root. For the LWD EM applications, we choose the integration interval for quasi-optimal sampling as $[-1.0, -1.0e^{-5}]\cup[1.0e^{-5}, 1.0]$. To validate Eq.(A-6), we compute the left side ($R_n(s)$) and the right side ($F(s)$) with respect to s, respectively. The relative error $|R_n(s)/F(s) - 1|$ is shown in Fig.A-1. It can be observed that all relative errors between $R_n(s)$ and $F(s)$ are smaller than 1.0% within the full sampling section, indicating that the rational function is reasonable.

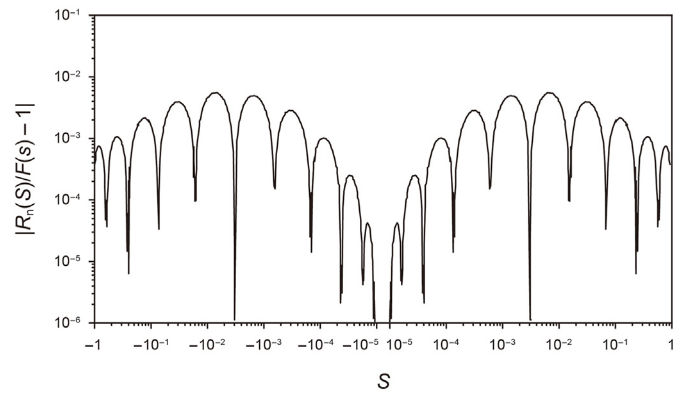

Fig. A. 1 Relative error of $|R_n(s)/F(s) - 1|$.

References

Abubakar, A., Habashy, T.M., Druskin, V.L., Knizhnerman, L., Alumbaugh, D., 2008. 2.5D forward and inverse modeling for interpreting low-frequency electromagnetic measurements. Geophysics 73 (4), 165–177. https://doi.org/10.1190/1.2937466.

Antonsen, F., Olsen, P.A., Stalheim, S.O., Constable, M.V., Irondelle, M., Cook, M., Bjorstad, T.R., Dupuis, C., Marza, P., Seydoux, J., Omeragic, D., 2014. Net Pay Optimization and Improved Reservoir Mapping from Ultra-deep Look Around LWD-Measurements. Abu Dhabi International Petroleum Exhibition and Conference. Society of Petroleum Engineers.

Bell, C., Hampson, J., Eadsforth, P., Chemali, R.E., Helgesen, T.B., Meyer, W.H., Randall, R., Peveto, C., Poppitt, A., Signorelli, J., Wang, T., 2006. Navigating and Imaging in Complex Geology with Azimuthal Propagation Resistivity while Drilling. In: SPE Annu. Tech. Conf. Exhib. Society of Petroleum Engineers.

Bittar, M.S., Klein, J.D., Randy, B., Hu, G., Wu, M., Pitcher, J.L., Golla, C., Althoff, G.D., Sitka, M., Minosyan, V., Paulk, M.D., 2009. A new azimuthal deep-reading resistivity tool for geosteering and advanced formation evaluation. SPE Reservoir Eval. Eng. 12 (2), 270–279. https://doi.org/10.2118/109971-PA.

Chaumont-Frelet, T., Pardo, D., Rodríguez-Rozas, Á., 2018. Finite element simulations of logging-while-drilling and extra-deep azimuthal resistivity measurements using non-fitting grids. Comput. Geosci. 22 (5), 1161–1174. https://doi.org/10.1007/s10596-018-9744-6.

Chen, Y.H., Omeragic, D., Druskin, V., Kuo, C.H., Habashy, T., Abubakar, A., Knizhnerman, L., 2011. 2.5D FD Modeling of EM Directional Propagation Tools in High-Angle and Horizontal Wells. SEG Annu. Meeting. Society of Exploration Geophysicists.

Davydycheva, S., Druskin, V., Habashy, T., 2003. An efficient finite-difference scheme for electromagnetic logging in 3D anisotropic inhomogeneous media finite-difference scheme in anisotropic media. Geophysics 68 (5), 1525–1536. https://doi.org/10.1190/1.1620626.

Dupuis, C., Omeragic, D., Chen, Y.H., Habashy, T., 2014. Inversion-based Workflow to Image Faults Crossed by the Wellbore Using Deep Directional Resistivity Provides New Way of Understanding Complex Formations. SPWLA 55th Annu. Logging Symp. Society of Petrophysicists and Well-Log Analysts.

Hartmann, A., Vianna, A., Maurer, H.M., Sviridov, M., Martakov, S., Lautenschläger, U., Antonsen, F., Olsen, P.A., Constable, M.V., 2014. Verification Testing of a New Extra-deep Azimuthal Resistivity Measurement. SPWLA 55th Annu. Logging Symp. Society of Petrophysicists and Well-Log Analysts.

Hawkins, D., Phettongkam, N., Nakchamnan, N., 2015. Optimizing well placement in geosteering using an azimuthal resistivity tool in complex thin bed reservoirs in the Gulf of Thailand. SPWLA 56th Annu. Logging Symp. Society of Petrophysicists and Well-Log Analysts.

Hong, D.C., Xiao, J.Q., Zhang, G.Y., Yang, S.D., 2013. Characteristics of the sum of cross-components of triaxial induction logging tool in layered anisotropic formation. IEEE Trans. Geosci. Rem. Sens. 52 (6), 3107–3115. https://doi.org/10.1109/TGRS.2013.2269714.

Hong, D.C., Li, N., Han, W., Zhan, Q.W., Zeyde, K., Liu, Q.H., 2021. An analytic algorithm for dipole electromagnetic field in fully anisotropic planar-stratified media. IEEE Trans. Geosci. Rem. Sens. 59 (11), 9120–9131. https://doi.org/10.1109/TGRS.2020.3040193.

Hu, Y.Y., Fang, Y., Wang, D.Z., Zhong, Y., Liu, Q.H., 2018. Electromagnetic waves in multilayered generalized anisotropic media. IEEE Trans. Geosci. Rem. Sens. 56 (10), 5758–5766. https://doi.org/10.1109/TGRS.2018.2825430.

Ingerman, D., Druskin, V., Knizhnerman, L., 2000. Optimal finite difference grids and rational approximations of the square root I. Elliptic problems. Commun. Pure Appl. Math. 53, 1039–1066. https://doi.org/10.1002/1097-0312(200008)53:8<1039::AID-CPA4>3.0.CO;2-I.

Lebedev, V.I., 1964. Difference analogues of orthogonal decompositions, basic differential operators and some boundary problems of mathematical physics. I. USSR Comp. Math. Math. 4 (3), 449–465. https://doi.org/10.1016/0041-5553(64)90240-X.

Lee, H.O., Teixeira, F.L., 2007. Cylindrical FDTD analysis of LWD tools through anisotropic dipping-layered earth media. IEEE Trans. Geosci. Rem. Sens. 45 (2), 383–388. https://doi.org/10.1109/TGRS.2006.888139.

Li, Q.M., Omeragic, D., Chou, L., Yang, L.B., Duong, K., 2005. New directional electromagnetic tool for proactive geosteering and accurate formation evaluation while drilling. SPWLA 46th Annu. Logging Symp. Society of Petrophysicists and Well-Log Analysts.

Li, M., Druskin, V., Abubakar, A., Habashy, T.M., 2016. A 2.5 D finite-difference algorithm for elastic wave modeling using near-optimal quadratures. Geophysics 81 (4), T155–T162. https://doi.org/10.1190/geo2015-0550.1.

Li, H., Wang, H., Wang, L., Zhou, X.T., 2020. A modified Boltzmann Annealing Differential Evolution algorithm for inversion of directional resistivity logging-while-drilling measurements. J. Petrol. Sci. Eng. 188, 106916. https://doi.org/10.1016/j.petrol.2020.106916.

Løseth, L.O., Ursin, B., 2007. Electromagnetic fields in planarly layered anisotropic media. Geophys. J. Int. 170 (1), 44–80. https://doi.org/10.1111/j.1365-246X.2007.03390.x.

Omeragic, D., Habashy, T., Esmersoy, C., Li, Q.M., Seydoux, J., 2006. Real-time Interpretation of Formation Structure from Directional EM Measurements. SPWLA 47th Annu. Logging Symp. Society of Petrophysicists and Well-Log Analysts.

Pardo, D., Torres-Verdín, 2015. Fast 1D inversion of logging-while-drilling resistivity measurements for improved estimation of formation resistivity in high-angle and horizontal wells. Geophysics 80 (2), E111–E124. https://doi.org/10.1190/geo2014-0211.1.

Seydoux, J., Legendre, E., Mirto, E., Dupuis, C., Denichou, J.M., Bennett, N., Kutiev, G., Kuchenbecker, M., Morriss, C., Yang, L., 2014. Full 3D deep directional resistivity measurements optimize well placement and provide reservoir-scale imaging while drilling. In: SPWLA 55th Annu. Logging Symp. Society of Petrophysicists and Well-Log Analysts.

Sun, Q.T., Hu, Y.Y., 2021. Fast geometric multigrid preconditioned finite difference frequency-domain method for borehole electromagnetic sensing. IEEE Geosci. Remote S 19, 8007404. https://doi.org/10.1109/LGRS.2021.3053590.

Thiel, M., Omeragic, D., 2017. High-fidelity real-time imaging with electromagnetic logging-while-drilling measurements. IEEE Trans. Comput. Imaging 3 (2), 369–378. https://doi.org/10.1109/TCI.2017.2670364.

Wang, L., Li, H., Fan, Y.R., 2019. Bayesian inversion of logging-while-drilling extra-deep directional resistivity measurement using parallel tempering Markov chain Monte Carlo sampling. IEEE Trans. Geosci. Rem. Sens. 57 (10), 8026–8036. https://doi.org/10.1109/TGRS.2019.2917839.

Wang, L., Deng, S.G., Xie, G.B., Li, S.J., Wu, Z.G., Fan, Y.R., 2022. A new deep-reading look-ahead method in electromagnetic logging- while-drilling using the scattered electric field from magnetic dipole antennas. Petrol. Sci. 19 (1), 180–188. https://doi.org/10.1016/j.petsci.2021.09.035.

Wu, H.H., Golla, C., Parker, T., Clegg, N., Monteilhet, L., 2018. A new ultra-deep azimuthal electromagnetic LWD sensor for reservoir insight. In: SPWLA 59th Annu. Logging Symp. Society of Petrophysicists and Well-Log Analysts.

Wu, Z.G., Fan, Y.R., Wang, J.W., Zhang, R.R., Liu, Q.H., 2020. Application of 2.5-D finite difference method in Logging-While-Drilling electromagnetic measurements for complex scenarios. IEEE Geosci. Remote S. 17 (4), 577–581. https://doi.org/10.1109/LGRS.2019.2926740.

Yan, L., Shen, Q.Y., Lu, H., Wang, H.M., Fu, X., Chen, J.F., 2020. Inversion and uncertainty assessment of ultra-deep azimuthal resistivity logging-while-drilling measurements using particle swarm optimization. J. Appl. Geophys. 178, 104059. https://doi.org/10.1016/j.jappgeo.2020.104059.

Yee, K., 1966. Numerical solution of initial boundary value problems involving Maxwell's equations in isotropic media. IEEE Trans. Antenn. Propag. 14 (3), 302–307. https://doi.org/10.1109/TAP.1966.1138693.

Zeng, S.B., Chen, F.Z., Li, D.W., Chen, J., Chen, J.F., 2018. A novel 2.5 D finite difference scheme for simulations of resistivity logging in anisotropic media. J. Appl. Geophys. 150, 144–152. https://doi.org/10.1016/j.jappgeo.2018.01.021.

Zhou, J., Li, H., Rabinovich, M., D'Arcy, B., 2016. Interpretation of Azimuthal Propagation Resistivity Measurements: Modeling, Inversion, Application and Discussion. SPWLA 57th Annu. Logging Symp. Society of Petrophysicists and Well-Log Analysts.